Experimental Mechanics
https://doi.org/10.1007/s11340-019-00532-0

# A Novel *In Situ* Experiment to Investigate Wear Mechanisms in Biomaterials

N. Alderete[1] · A. Zaheri[1] · H.D. Espinosa[1,2]

Received: 7 February 2019 / Accepted: 17 June 2019
© Society for Experimental Mechanics 2019

**Abstract**
A number of experimental techniques have been used to characterize the mechanical properties and wear of biomaterials, from nanoindentation to scratch to atomic force microscopy testing. While all these experiments provide valuable information on the mechanics and functionality of biomaterials (e.g., animals' teeth), they lack the ability to combine the measurement of force and sliding velocities with high resolution imaging of the processes taking place at the biomaterial-substrate interface. Here we present an experiment for the *in situ* scanning electron microscopy characterization of the mechanics of friction and wear of biomaterials with simultaneous control of mechanical and kinematic variables. To illustrate the experimental methodology, we report the wear of the sea urchin tooth, which exhibits a unique combination of architecture and material properties tailored to withstand abrasion loads in different directions. By quantifying contact conditions and changes in the tooth tip geometry, we show that the developed methodology provides a versatile and promising tool to investigate wear mechanisms in a variety of animal teeth accounting for microscale effects.

**Keywords** Wear · *In situ* experimentation · Biomaterials

## Introduction

Heavily mineralized biological materials, examples of which can be encountered in mollusk shells, bones and teeth, have been the subject of numerous structural and mechanistic studies seeking models for engineering composite analogues [1]. Animal teeth, in particular, have received significant attention over recent years on account of their wearing and damage tolerance mechanisms [2–5]. Depending on the nature of the teeth's functionality, various strategies have been employed, by natural design, to give rise to extraordinary degrees of performance in mechanical and tribological properties (e.g., abrasion tolerance, fracture toughness and impact resistance) [6]. Mammalian teeth, for example, use a combination of a hard enamel coating on a soft dentin substrate, resulting in an interface that serves as a crack arresting barrier [6], a feature that is better understood when coupled with the piercing and biting functionalities of these elements [7]. In contrast to piercing and biting, grinding is the predominant form of motion in the teeth of terrestrial and aquatic herbivores [8], and is often found in combination with the other motions in the dental systems of omnivores [9]. Naturally, motion and contacts in dentition cause wearing of the teeth, a time-augmenting phenomenon which requires control during the lifetime of the animal to guarantee its survival. Millions of years of evolution have contributed to selecting and enhancing natural mechanisms to control abrasive wear by continuous growth, replacement of the damaged fragments and self-wearing [10–12]. Such capabilities are often deemed as self-sharpening and represent a rich source of natural inspiration for the manufacturing of advanced cutting tools. Multiple species in the animal kingdom have been recently identified to be endowed with self-sharpening competence.

One of the finest examples is posed by the sharpening mechanisms of the chiton's teeth (Fig. 1(a)), a fish which grazes the underwater rocky surfaces in pursuit of nourishment. The mechanism was depicted as the wearing of the

N. Alderete and A. Zaheri contributed equally to this work.

**Electronic supplementary material** The online version of this article (https://doi.org/10.1007/s11340-019-00532-0) contains supplementary material, which is available to authorized users.

✉ H.D. Espinosa
espinosa@northwestern.edu

[1] Theoretical and Applied Mechanics Program, Northwestern University, 2145 Sheridan Rd., Evanston, IL 60208-3109, USA

[2] Department of Mechanical Engineering, Northwestern University, 2145 Sheridan Rd., Evanston, IL 60208-3109, USA

Published online: 15 July 2019

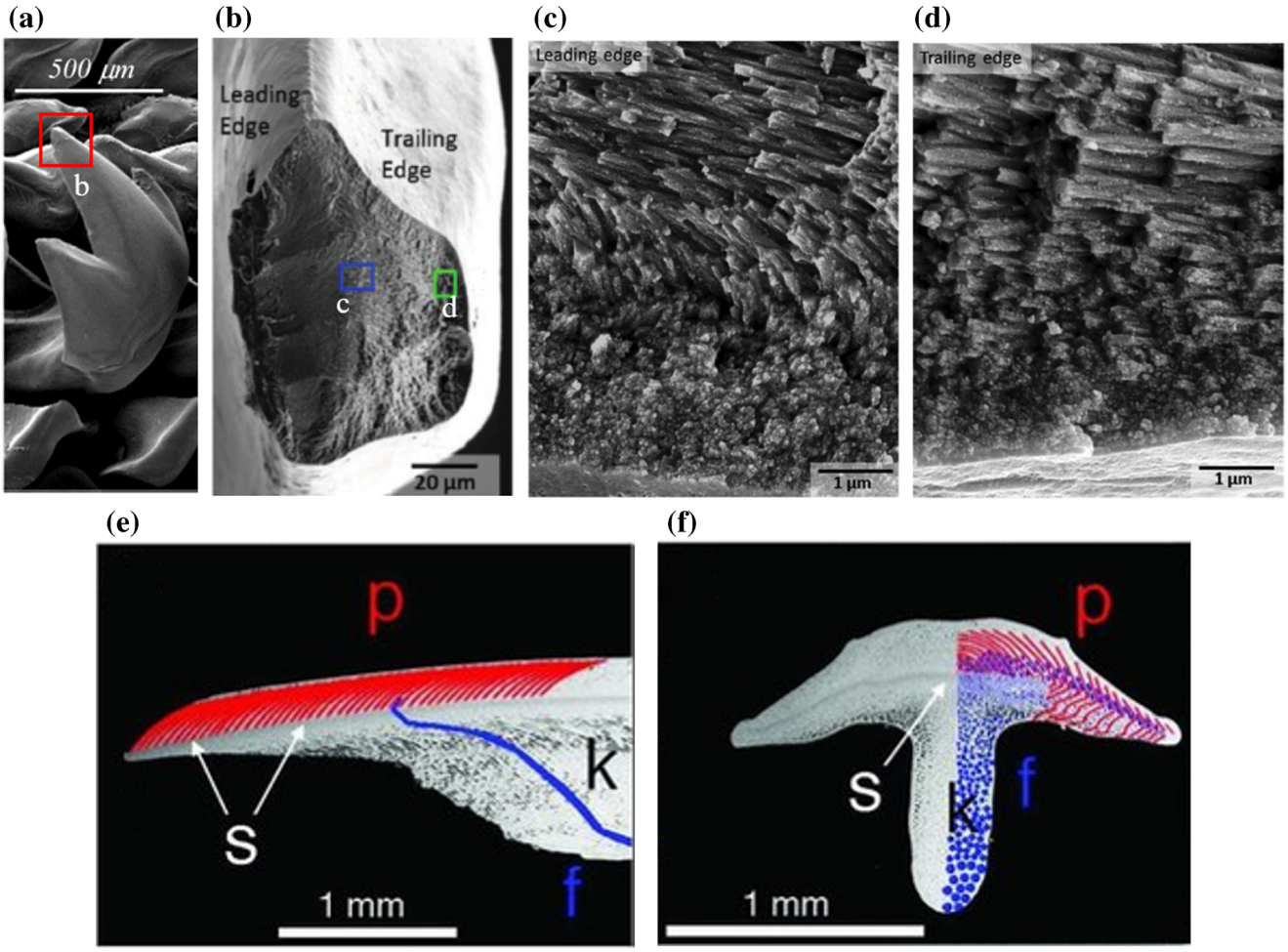


**Fig. 1** A chiton tooth [16] (**a**) A whole tooth. (**b**) SEM image of the latitudinal fracture near the tip of the tooth. Micrograph of the longitudinal fracture surface: (**c**) Leading edge with thick nanoparticulate layer and rotating nanorods. (**d**) Trailing edge with thin nanoparticulate layer and singly oriented nanorods. SEM images of a sea urchin tooth [19]. (**e**) Longitudinal view of the tooth showing T-shape structure. (**f**) Etched cross-section of the tooth highlighting structural components (Plates: P, Stone: S, Fibers: f and Keel: K)

anterior surface of the cusp while maintaining a sharp posterior cutting edge [13]. Chiton teeth are mineralized with a range of iron oxides including magnetite [14, 15]. The multiscale structure of the tooth is depicted in Fig. 1. For scraping purposes, the teeth are designed with a concavely-bent front side, which acts as the leading edge, and a convexly-bent rear side that serves as the trailing edge (Fig. 1(b)) [16]. The leading edge is comprised of regions of dense magnetite-nanoparticles embedded in a chitin-based matrix (Fig. 1(c)). The nanoparticle morphology abruptly transitions (within 1 μm) into a predominantly magnetite-nanorods region, where rotation of the rods tends towards alignment with the tooth's long axis. In the trailing edge, on the other hand, nanoparticulate regions of less density are observed, together with wider nanorods (~1.3 times greater) and no significant orientation changes (Fig. 1(d)). The layers of aligned, hexagonal close-packed, rod-like elements consist of randomly oriented crystallites. This feature distinguishes the chiton teeth as possessing "the highest hardness of any reported biomineral" [17], a property that inspires the development of novel abrasion-resistance materials.

Similarly, the self-sharpening capability was identified in the incisors of beavers, who use their teeth to cut trees and plants. It was shown that the optimized wedge angle in the geometry of the rodent's teeth along with the existence of a harder layer (i.e., enamel) on top of a softer one (i.e., dentin) could lead to the self-sharpening of the wedge [18].

In addition, researchers hypothesized a self-sharpening mechanism on sea urchin teeth, Fig. 1(e–f), from images of fracture on the convex region of the teeth [19]. Radial and lateral motions of the teeth against hard surfaces have been hypothesized to cause abrasion, which leads to the shedding of primary plates and fibers, and a subsequent renewal process that ultimately gives rise to the sharpening of the teeth. The above studies lacked direct imaging of the wear and self-sharpening processes within an experimental setting that closely mimics conditions found in nature. They also lacked measurements of mechanical variables needed to enable

characterization of such mechanisms including wear rate, influence of external effects on wear (e.g., substrate/tooth hardness, friction coefficient, and applied normal load), wear directionality, and its relation with microstructural features. Here we present an experimental methodology suited to address such gap.

## Experimental Methods to Study the Wear of Biological Materials

A copious amount of experimental methods have been developed and employed to gain insight on wear mechanisms and quantify wear-induced-damage tolerance, especially on a variety of biological hard tissues. Similar to the techniques used for metallic and polymeric materials [20], mechanistic frameworks and subsequent property maps, based on the two-body interaction system, have been developed for biological materials. In this particular context, the bio-material is commonly employed as a flat substrate onto which indentations are performed by a rigid material (e.g., diamond). By means of systematic indentation, abrasion maps were generated for different criteria, based on the yielding and cracking damage of the contacts, as well as ratios of mechanical variables such as: hardness, elastic moduli, and fracture toughness [21]. These maps are useful in comparing the abrasion and wear performance of different families of tissues. Notwithstanding, the tribological dependence on environmental and loading conditions (i.e., load regimes and contact geometries), restricts the applicability of abrasion maps and dictates a cautionary approach to their use. An alternative to such an experimental approach is posed by nanoscale scratching of biological samples. By employing lateral force modes in atomic force microscopy (AFM), friction measurements have been conducted on human teeth, marine Nereis worms and grasshopper mandibles in dry and hydrated conditions [2]. Among the findings, it was reported that the highest removal of material was observed for the dry hard material, demonstrating that the hardness to elastic modulus ratio does not constitute a reliable measure of abrasion resistance. In another work, the triboindenting capability of in-situ scanning probe microscopy (SPM) was exploited to study the wear resistance of marine warm jaws [3]. The authors drew a correlation between the chemical composition and mechanical properties as well as wear resistance; yet a conflicting effect of nano-scale wear on localized regions of the jaws was detected under hydrated conditions [4]. In another attempt, the deformation mechanism of the stone region in a sea urchin tooth was investigated through a combination of nano-scratching and transmission electron microscopy (TEM), only to reveal a variety of mechanisms which included twinning and crack propagation. Furthermore, energy dissipation in the stone region was described in relation to its components (i.e., fibers, matrix and interfaces) [22]. Nevertheless, the aforementioned experimental methodologies can only assess wear resistance and surface deformation under frictional contact, while failing to account for more complex loading conditions and biomechanical functionalities encountered in Nature. This calls for the development of novel experiments providing a versatile control of loading conditions, relative sliding speeds, and direct imaging capabilities to evaluate wear-related phenomena in bio-materials systems, in both a qualitative and quantitative fashion.

## *In-Situ* SEM Wear Experiment

### Concept and Experimental Setup

A novel in-situ SEM wear test was developed to characterize the tribological behavior and wear mechanisms in biomaterials with animal teeth as a case study. The developed scratching methodology seeks to mimic the actual kinematic features of the tooth grinding process and reveal the underlying wearing mechanism without resorting to indirect abrasion and damage measurements resulting from the application of stress on their surface.

In-situ wear tests were carried out by employing a commercial Alemnis® nano-mechanical indenter inside the chamber of a Nova NanoSEM 600 SEM operating at 10 kV and 2.6 nA. The Alemnis nanoindenter, shown in Fig. 2(a), allows to perform a variety of mechanical tests (e.g., tension, compression, scratching) while continuously recording the load and displacement and, when used in the in-situ mode, imaging of deformation mechanisms as they occur. In the Alemnis apparatus, a piezoelectric actuator applies a controlled displacement to the indenter tip as a response to the application of an external voltage. The resulting enforced displacement is measured by a displacement sensor located on the indenter head (1 nm RMS noise at 200 Hz.). As the indenter engages the sample, the resulting load is measured by the load sensor located underneath the sample (4μN RMS noise at 200 Hz.). A set of orthogonal piezo-actuators attached to the z-axis load sensor allow for in-plane x-y translation degrees of freedom, which complement the out-of-plane z-motion of the indenter head. The piezoelectric nature of the displacement actuator implies true displacement control (1 nm RMS noise at 200 Hz) unlike indenters that employ load control with displacement feedback.

In the wear tests, the tooth was mounted in an ad-hoc customized tip-holder (to accommodate the geometry and physical characteristics of the sample) while an ultrananocrystalline diamond (UNCD) thin film (~1$\mu m$ thick) deposited on a silicon wafer was mounted on top the load sensor (Fig. 2). The diamond substrate was selected to act as a rigid, non-wearing, non-deformable surface,

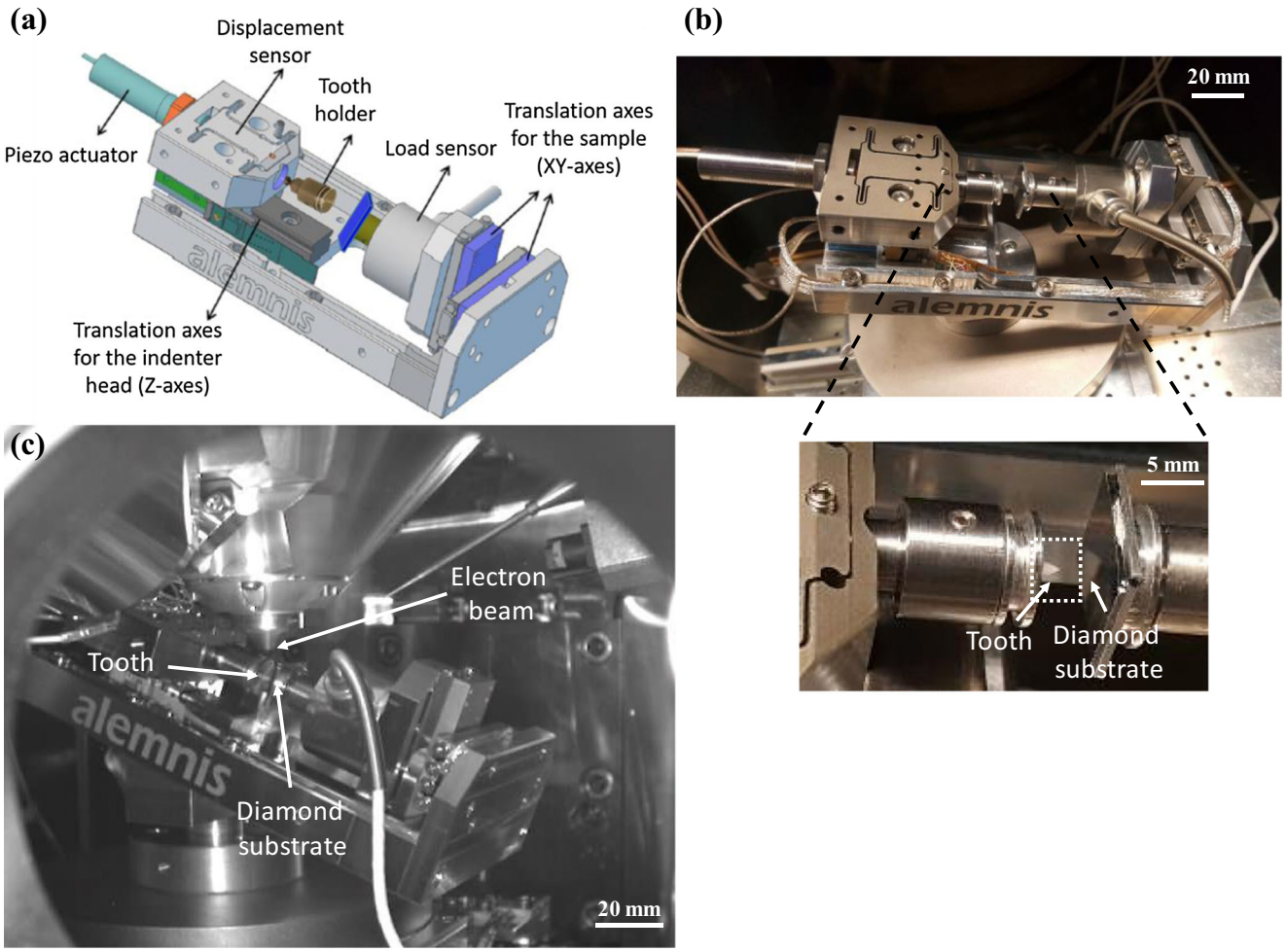


**Fig. 2** (**a**) Schematic of the Alemnis indenter showing the different components; (**b**) Setup of the tester with the mounted tooth (see zoomed view in the inset of (**b**)) and the substrate on the SEM stage; (**c**) The whole setup inside the SEM chamber showing the electron beam scanned over the tooth and the diamond substrate

thus isolating the wearing phenomena exclusively to the tooth. The assembly was then placed into the chamber of an SEM and oriented so that the incident electron beam can be scanned within the region where the sample and the substrate engage during scratching, Fig. 2(c). Contrary to conventional scratch testing methodologies, where the substrate is the sample of interest and a diamond tip is employed to apply the scratching load; the experimental setup depicted in Fig. 2(a) allowed the tooth to be the scratching element. This particular arrangement granted the experiment with the capability of mimicking actual abrading and scraping motion found in teeth, while conveniently enabling the investigation of tooth wear mechanisms.

## Dimensional Analysis

A dimensional analysis was carried out to systematically relate the experimentally observed wear to the various variables. The advantage of non-dimensional forms rests on the identification of group of variables on which the wear depends on. It also allows for the selection of different experimental conditions and extension to teeth wear of different animal species. In our formulation, Wear ($w$) is considered a function of six variables, namely: Applied Normal Load ($F_N$), Kinematic Friction Coefficient ($\mu$), Sliding Speed ($V_{Sliding}$), Sliding Duration ($t_{Sliding}$), Tooth Hardness ($H_{Tooth}$) and Effective Contact Radius ($a$), the latter derived from Hertzian contact mechanics. Namely,

$$w = f\left(F_N, \mu, V_{Sliding}, t_{Sliding}, H_{Tooth}, a\right) \tag{1}$$

Application of Buckingam's Pi Theorem allows grouping of the variables into four dimensionless numbers ($\pi_i$), viz.,

$$\pi_1 = H_{Tooth}^{x_1}\, a^{y_1}\, V^{z_1}\, \mu \tag{2a}$$

$$\pi_2 = H_{Tooth}^{x_2}\, a^{y_2}\, V^{z_2}\, F_N \tag{2b}$$

$$\pi_3 = H_{Tooth}^{x_3}\, a^{y_3}\, V^{z_3}\, t \tag{2c}$$

$$\pi_4 = H_{Tooth}^{x_4}\, a^{y_4}\, V^{z_4}\, w^{i} \tag{2d}$$

Summation of the powers ($x_i$, $y_i$, $z_i$) of the corresponding fundamental units (i.e., time, mass, length) yields the reduced form of the functional relation of equation (1):

$$\frac{w^i}{a^i} = f\left(\mu, \frac{L}{a_0}, \frac{F_N}{a^2 H_{tooth}}\right) \tag{3}$$

Spatial dimensionality in the dimensional functional form is introduced by the $i$ superscripts (and powers) where, for the two-dimensional case the wear parameter ($w$) is given by the Flattened Area ($A_{fl}$) and $i$ adopts the value of 2. Similarly, for the three-dimensional case the wear parameter (w) is given by the chipped volume ($V_{cp}$) and $i$ is 3. Inspection of equation (2) allows to interpret $F_N/a^2$ as the applied nominal contact stress and the sliding length ($L$) as the product of the kinematic conditions during the sliding procedure (i.e., $V_{Sliding}$x $t_{Sliding}$).

## Test Procedure

The experimental procedure is guided by the dimensional analysis, equation (3). Changing the substrate material allows the investigation of the friction coefficient, changing the sliding velocity or sliding time enables investigation of the effect of scratch distance, and changing $F_N/a^2$ provides information on the effect of the contact stress.

After the assembly is inside the SEM, the sample and the substrate are brought to a distance of about 0.3 μm, from which the experiment can start. A holding time to stabilize the various noise sources within the system (e.g., thermal drift) is recommended. SEM images of the tooth tip in contact with the diamond substrate are acquired, see Fig. 3(a–b). The applied compression load and sliding velocity follow the trapezoidal and rectangular profiles shown in Fig. 3(c), respectively. First, a compression ramp is applied during 20s until a target compression load is reached. This compression load is held constant throughout the scratching phase via load control. Immediately after reaching the target load and after completion of the scratching portion of the test (prior to unloading), the compression load is held for 10s to ensure proper realization of the target compressive stress and post-scratching relaxation. The target compression load is calculated following a classical Hertzian contact mechanics analysis for elastic circular contacts, enforcing a target contact stress $\sigma_t$ (typically multiples of the yield stress) in which the tooth is idealized as a rounded body corresponding to its natural geometry and the substrate as a rigid half-space, as described by equation (4):

$$\sigma_t = \frac{1}{\pi}\left\{\frac{6F_N}{R_{Tooth}}\left[\frac{E_T}{(1-\nu_T^2) + \frac{E_T}{E_S}(1-\nu_S^2)}\right]\right\}^{\frac{1}{3}} \tag{4}$$

The imposed velocity during sliding is 10 μm/s, which is kept constant during the experiment over a sliding distance of 1000 $\mu m$. Scratch velocity and scratch length are chosen to ensure stable friction regimes and to comply with limitations stemming from the experimental setup (i.e., displacement range of the Alemnis indenter and video capture rate of the SEM camera for adequate visualization of the wear process). Stability of the frictional regime was evaluated via a series of scratching tests performed on an MTS Nanoindenter, on at least four different teeth and at two different levels of normal force (i.e., 10 mN and 100 mN) and sliding velocity (i.e., 1 μm/s and 10 μm/s), see Fig. 3(d). Furthermore, it is noted that during scratching the diamond substrate is moving against the tooth while the applied normal force is kept constant on the tooth. All tests are recorded to fully capture the wear process.

To maintain an approximately constant contact stress, each test was performed in a series of subsequent sliding steps. After each step, consisting of a sliding distance of 1000 μm, the tooth was removed from the setup, re-coated with $OsO_4$ and imaged in an SEM to enable digital measurements of the regions of interest (i.e., worn regions). Image post-processing software was used to compute the flattened areas ($A_{fl}$) (see blue colored regions in Fig. 4). From the measured flattened area, a new applied normal force was obtained for the subsequent sliding increment. The thickness of chipped plates and chipped volumes ($V_{cp}$) were also calculated.

## A case study: wear results for the sea urchin teeth

Teeth were separated from the Aristotle's lantern of frozen pink sea urchins (*Strongylocentrotus fragilis*) at room temperature. They were rinsed in distilled water and dried out at room temperature. Segments of 4-5 mm in length, measured from the grinding tip, were excised from the teeth using a razor blade. The length restriction avoids excessive bending or buckling of the samples when in contact with- and pressed and scratched against the diamond substrate. Selection of pristine teeth is conducted by optical microscope inspection, after which samples were mounted in customized holders and held in place by use of a commercial epoxy adhesive (Loctite 1C Hysol Epoxi-Patch). Given the biological nature of the samples, 8 nm Osmium coating was applied for appropriate SEM imaging of pristine samples and 4 nm coating for subsequent imaging of scratch-damaged samples.

Two modes of motions for the teeth are considered here. The first motion, henceforth called radial, is parallel to the keel part the tooth. The second motion of the teeth, henceforth called lateral, lies perpendicular to the same part. The radial direction corresponds to the scraping and biting movements of the echinoderm, whereas the lateral direction is associated to the motion observed in the Aristotle's lantern, which holds the entire set of

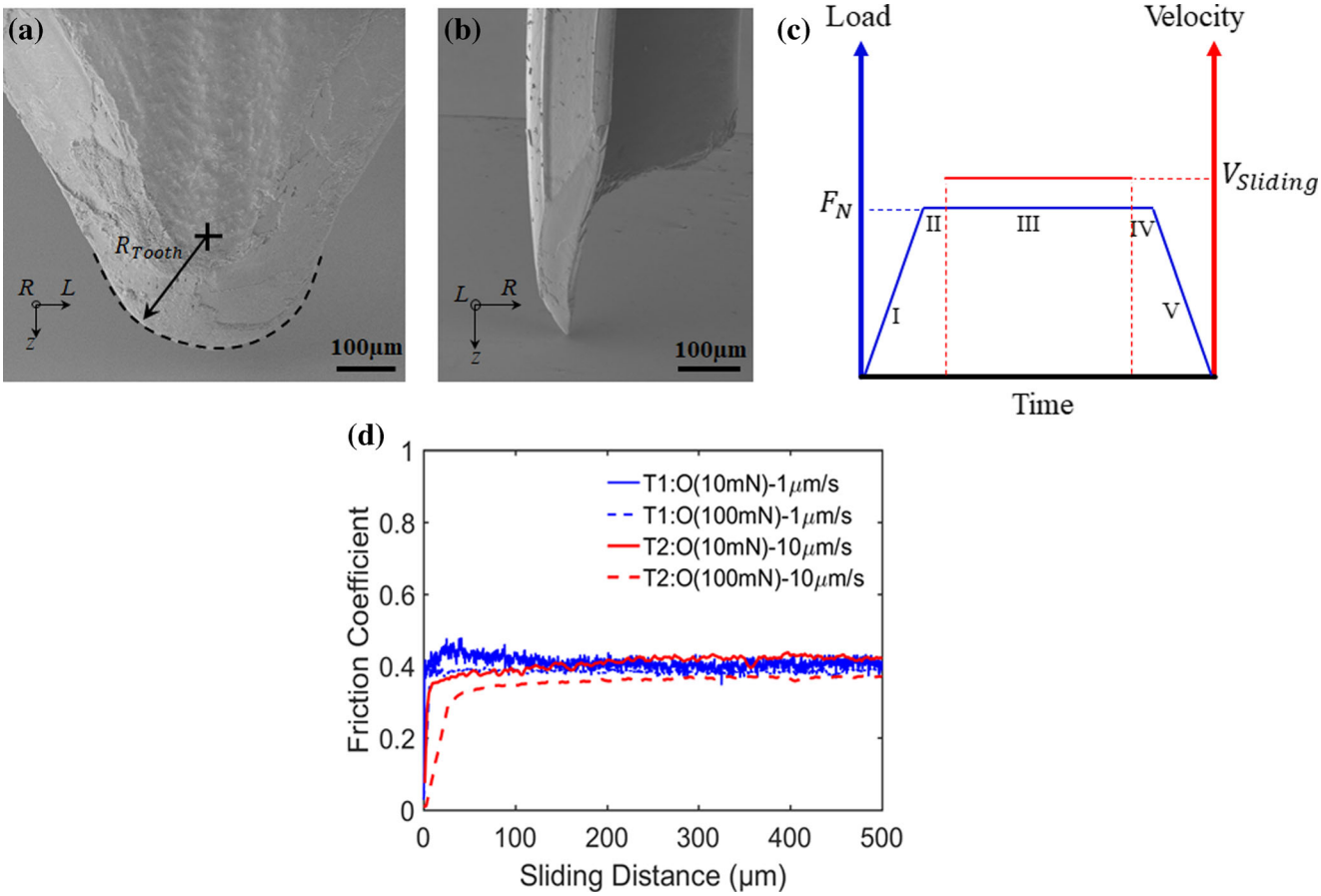


**Fig. 3** (**a**) An SEM image of the tooth tip from the convex side with highlighted tooth curvature. (**b**) An SEM image of the tooth tip from the lateral viewpoint in contact with the diamond substrate. (**c**) Applied normal load and velocity profiles of the sliding experiments (segments of the loading profile are: I) Loading, II) Holding before initiation of sliding, III) Holding the load constant during sliding IV) Holding with sliding stopped and V) Unloading). (**d**) Analysis of friction coefficient variation with sliding distance under two different levels of sliding velocities and normal forces

teeth in the mouthpart. Previously, it was observed that both motions might abrade the sides of the teeth during their working time [19]. To examine the role of directional loading on the wearing of the teeth, in-situ wear tests under constant stress were conducted. The contact stress was selected to deliver a mean pressure equivalent to the yield stress of the tooth, to ensure that no cracks would initiate during the initial penetration against the diamond substrate [23].

Teeth for each sliding direction were prepared and their tips characterized before and after each test through SEM imaging.

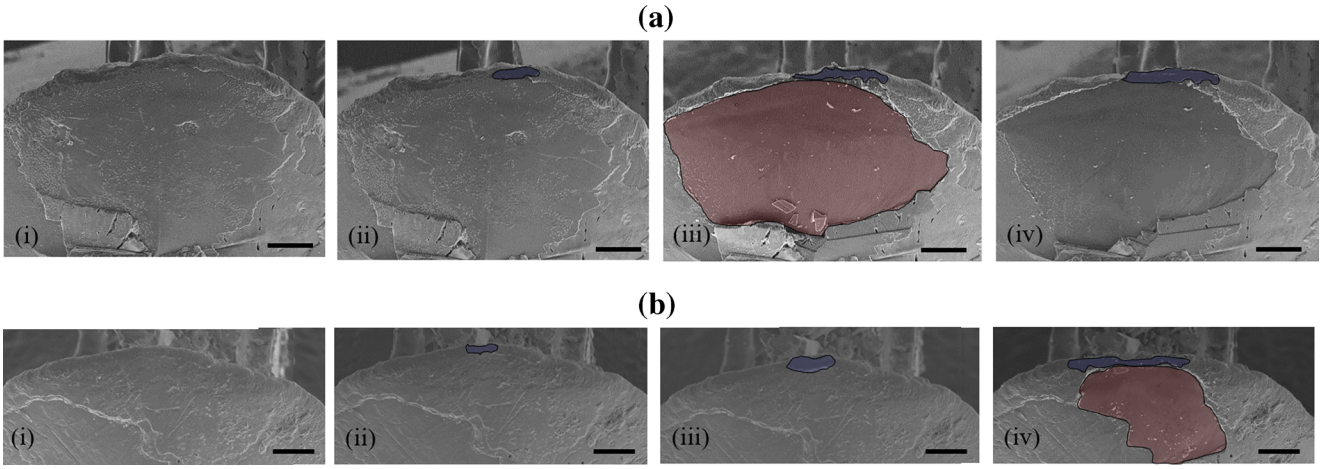


**Fig. 4** Characterization of the tip of the teeth before and after the scratch tests. SEM images of the tip of the teeth (Images from left to right in (**a**–**b**) correspond to increasing sliding distances, Scale bar: 40 µm). (**a**) Radial direction, (**b**) Lateral direction

Images of the pristine condition of two teeth are given in Fig. 4(a–b) in the first panel. These images depict the convex side of the teeth where the plates are stacked on top of each other. Following a few testing rounds, the teeth were taken out and imaged at the same orientation for the sake of comparison. The panels from left to right in Fig. 4 show the evolution of the teeth's tip from pristine condition up to severe flattening and chipping following several scratch-testing cycles in the radial, Fig. 4(a) and lateral directions, Fig. 4(b). The images revealed flattened areas as well as partial removal of the convex side of the tip. These regions were colored via image post-processing as blue and red for the former and latter, respectively.

One of the main advantages of performing *in situ* tests is the ability to capture the progression of the wear process in every scratch experiment (see for example movie in supporting document). Figure 5 shows the evolution of a single lateral scratch experiment captured in three distinct snapshots. Accumulation of debris from flattening of the contact area can be clearly observed as well as detachment of a significant mass of material corresponding to the primary plates' structure. The latter is evidenced by the characteristic brightness, indicative of the lack of Osmium coating.

Looking at the dimensional analysis introduced in equation (3), the friction coefficient, μ was the same for the both set of tests. In order to keep a second dimensionless group constant, $\frac{F_N}{a^2 H_{tooth}}$, the applied normal force was updated based on the new effective contact radius. This last parameter was obtained by quantifying the flattened area at the tip of the teeth using image post-processing. This provided the capability to keep the nominal contact pressure approximately constant over the entire sliding distance. Then, the dimensional wear parameter for both teeth was discriminated into two distinct manifestations (i.e., area flattening and volume chipping) and its relation to the normalized sliding distance, $L/a_0$, was investigated. Figure 6(a) plots the dimensional wear parameters of flattened area ($A_{fl}$) and chipped volume ($V_{cp}$) as a function of the adimensional characteristic length ($L/a_0$) for the two tested directions. Here, $w_R$ and $w_L$ refer to the wear parameters in the radial and lateral directions, respectively. The flattening area plots for both teeth show an increasing trend with increasing scratching length. These flattening areas correspond to the stone region at the tip of the teeth [23]. In addition, it can be observed that data points for the chipped volumes reveal a discontinuity following a certain amount of sliding. These chippings are associated to the removal of plates on the convex side of the tooth. Their volumes were calculated based on the highlighted areas multiplied by the thickness of the plates. By correlating the derived curves to the captured SEM images, it is clear that, at the chipping discontinuity, new plate surface emerges. Further examination of the flattened areas led to the understanding of the self-sharpening phenomenon [23]. In this regard, fracture of the plates on the convex side resulted in the reduction of the width of the flattened area. As a consequence, the profile of the tooth tip was preserved during progressive wear (self-sharpening mechanism fully discussed in [23]). To illustrate this feature, widths of the flattened regions ($w_f$) as a function of the normalized sliding distance are given in Fig. 6(b). The dropping points in the curves were attributed to the removal of plates and the sharpening of the tip. The same mechanisms were observed in both directions. Previously, we showed that this self-sharpening behavior is in utter contrast to the blunting process observed in scratching under a constant force condition [23].

## Wear Directionality

Tip imaging and wear quantification revealed a similar behavior with respect to the self-sharpening capability of the sea urchin tooth under both radial and lateral scratching, with abrasion being the dominant mode of wear. However, the rate of tip flattening and removal of plates is accelerated when the tooth is displaced in the lateral direction, Fig. 6. Close examination of the tooth tips following scratch testing reveals, however, that the failure mechanisms involved are intrinsically different on account of the load and material architecture directionality.

The SEM images in Fig. 7 present the damage evolution (from pristine condition to after a plate-shedding event) on laterally (a-c) and radially (d-f) scratched teeth. In contrast to

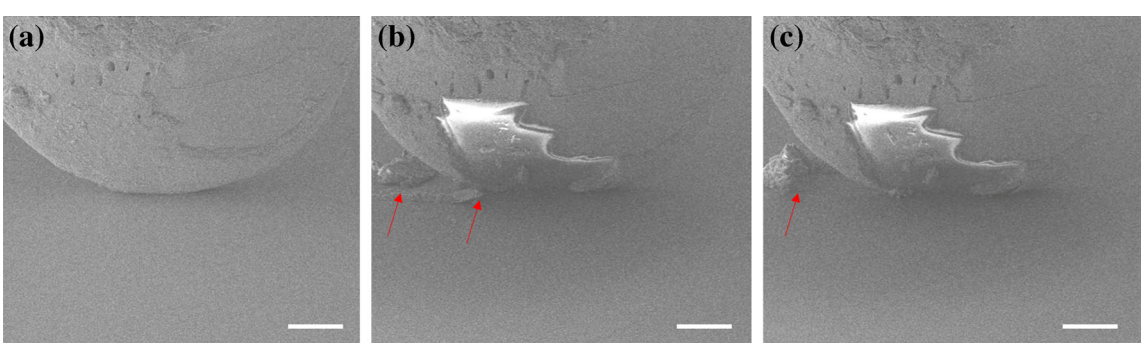


**Fig. 5** Snapshots of the recorded video (see supporting document) during the wear experiment inside the SEM chamber (Scale bar: 50 μm). (**a**) The pristine stage at the beginning of sliding. (**b**) and (**c**) different stages of sliding. The arrows indicate the detached debris from the stone region as well as the plates

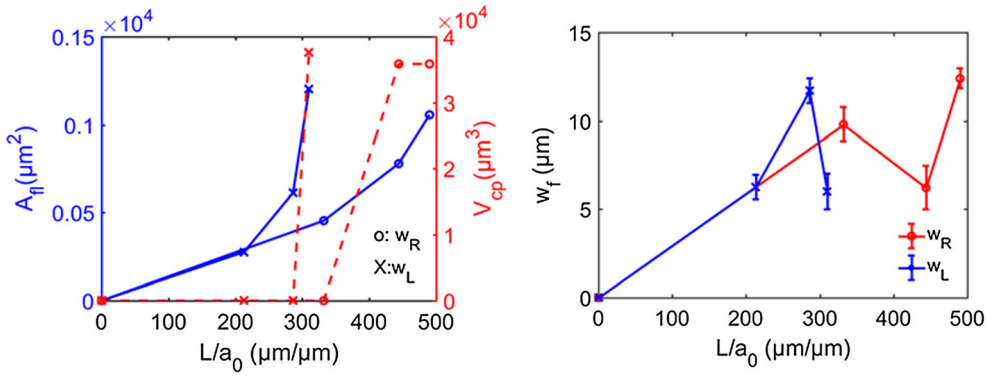


**Fig. 6** (**a**) Quantification of wear for both radial and lateral tooth motions. $A_{fl}$ and $V_{cp}$ refer to the flattened area of the tooth and the chipped volume of the plates as a function of normalized scratch length, $L/a_0$. (**b**) Measurement of width of the flattened regions ($w_f$) as a function of normalized scratch distance $L/a_0$. $w_R$ and $w_L$ refer to wear parameters in the radial and lateral directions, respectively

the radially scratched tooth, lateral scratching results in early exposure of stone fibers, coupled with fiber tearing, twisting, and fiber-matrix debonding. Stress concentration at the tip of the tooth is responsible for the initiation of cracks, whose propagation is favored by the weak organic interfaces between the plates. The differentiation factor is the direction of the shear stress relative to the orientation of the fibers in the stone and plate regions. During lateral scratching, damage induced by shear stresses gives rise to relative sliding, upon delamination and fiber-matrix debonding, analogous to the shearing of a deck of cards, which is consistent with typical failure patterns of ceramic fiber reinforced composites [24]. By contrast, in the radial direction, the shearing direction aligns with the longitudinal axis of the fibers. This is highlighted in the high magnification images of the stone region, taken after the scratch experiments, Fig. 7(c) and (f).

## Conclusions

A novel experimental method supported by a dimensional analysis framework was developed to characterize the

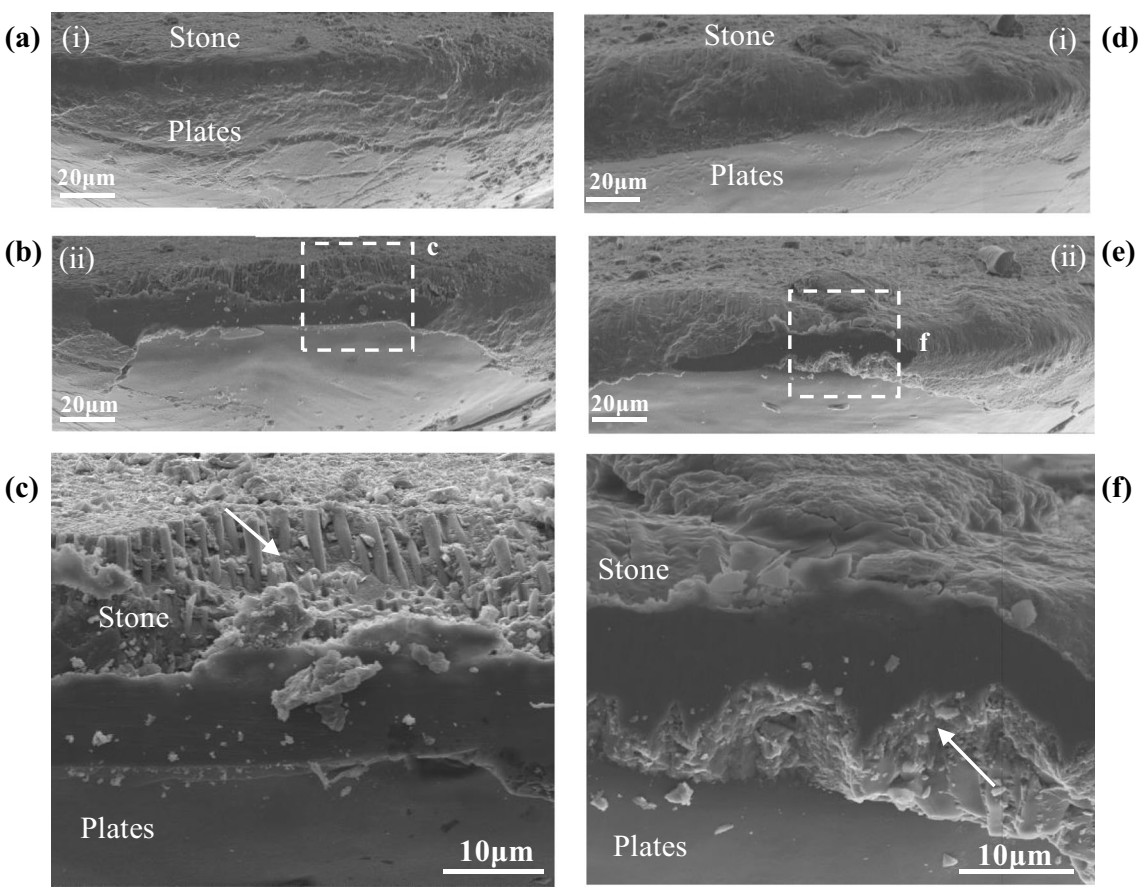


**Fig. 7** Characterization of the tip of the teeth before and after scratch tests in lateral (**a**–**c**) and radial (**d**–**f**) directions. (i) Corresponds to the pristine state and (ii) to the damaged states. The zoomed in images of the worn-out regions for both teeth are presented in (**c**) and (**f**)

tribological behavior and wear mechanisms in animal teeth. Successful implementation of the method enabled the investigation of the effect of contact stress, sliding distance, and scratch direction on the wear of sea urchin teeth, which is presented as a case study. Different wear rates and failure modes were observed for radial and lateral directions of motion, revealing the intrinsic relationship between material and microstructural design with loading direction. Comparison of the wear results for radial and lateral scratching reveals earlier departure from linearity, in the evolution of the flattened area for the lateral scratching, as well as earlier shedding of plates despite similarity in the chipped volumes.

While a variety of methods are available and have been applied to the study of similar phenomena, the proposed technique enables the recreation of more realistic scenarios, which more closely mimic the loading conditions and biofunctional features observed in biting, grinding and scraping of natural substrates. As such the experimental setup and protocols here reported are directly applicable to the investigation of wear mechanisms and its quantification in many species of interest. The developed dimensional model sheds light on the governing group of variables controlling wear and allows for a straightforward application to a variety of materials and loading conditions. Hence, the proposed framework is believed to constitute a significant step forward in the experimental study of wear mechanisms in animal teeth, whose ultimate value resides in the potential to develop Nature-inspired engineering tools for drilling, mining, and boring.

**Acknowledgements** The authors gratefully acknowledge financial support from a Multi-University Research Initiative through the Air Force Office of Scientific Research (AFOSR-FA9550-15-1-0009). A special thank is due to J. McKittrick and M. Frank for helpful discussions during the development of the experimental set up and for providing sea urchin teeth.

## References

1. Dunlop JWC, Fratzl P (2010) Biological composites. Annu Rev Mater Res 40:1–24
2. Schoberl T, Jager IL (2006) Wet or dry - hardness, stiffness and wear resistance of biological materials on the micron scale. Adv Eng Mater 8(11):1164–1169
3. Pontin MG, Moses DN, Waite JH, Zok FW (2007) A nonmineralized approach to abrasion-resistant biomaterials. Proc Natl Acad Sci 104(34):13559–13564
4. Moses DN, Pontin MG, Waite JH, Zok FW (2008) Effects of hydration on mechanical properties of a highly sclerotized tissue. Biophys J 94(8):3266–3272
5. Meng JX, Zhang PC, Wang ST (2016) Recent progress of abrasion-resistant materials: learning from nature. Chem Soc Rev 45(2):237–251
6. Imbeni V, Kruzic JJ, Marshall GW, Marshall SJ, Ritchie RO (2005) The dentin-enamel junction and the fracture of human teeth. Nat Mater 4(3):229–232
7. Walker A, Hoeck HN, Perez L (1978) Microwear of mammalian teeth as an Indicator of diet. Science 201(4359):908–910
8. Lawrence JM (2013) Sea urchins: biology and ecology, vol 38. Academic, San Diego
9. Bak RPM (1994) Sea-urchin bioerosion on coral-reefs - place in the carbonate budget and relevant variables. Coral Reefs 13(2):99–103
10. Ma Y, Weiner S, Addadi L (2007) Mineral deposition and crystal growth in the continuously forming teeth of sea urchins. Adv Funct Mater 17(15):2693–2700
11. Sone ED, Weiner S, Addadi L (2007) Biomineralization of limpet teeth: a cryo-TEM study of the organic matrix and the onset of mineral deposition. J Struct Biol 158(3):428–444
12. Erickson GM, Sidebottom MA, Curry JF, Ian Kay D, Kuhn-Hendricks S, Norell MA, Gregory Sawyer W, Krick BA (2016) Paleo-tribology: development of wear measurement techniques and a three-dimensional model revealing how grinding dentitions self-wear to enable functionality. Surface Topography-Metrology and Properties 4(2):024001
13. Shaw JA, Macey DJ, Brooker LR, Clode PL (2010) Tooth use and wear in three iron-biomineralizing Mollusc species. Biol Bull 218(2):132–144
14. Lowenstam HA (1962) Magnetite in denticle capping in recent hhitons (Polyplacophora). Geol Soc Am Bull 73(4):435
15. Gordon LM, Joester D (2011) Nanoscale chemical tomography of buried organic-inorganic interfaces in the chiton tooth. Nature 469(7329):194–197
16. Grunenfelder LK et al (2014) Stress and damage mitigation from oriented nanostructures within the Radular teeth of Cryptochiton stelleri. Adv Funct Mater 24(39):6093–6104
17. Weaver JC, Wang Q, Miserez A, Tantuccio A, Stromberg R, Bozhilov KN, Maxwell P, Nay R, Heier ST, DiMasi E, Kisailus D (2010) Analysis of an ultra hard magnetic biomineral in chiton radular teeth. Mater Today 13(1–2):42–52
18. Stefen C, Habersetzer J, Witzel U (2016) Biomechanical aspects of incisor action of beavers (Castor fiber L.). J Mammal 97(2):619–630
19. Killian CE, Metzler RA, Gong Y, Churchill TH, Olson IC, Trubetskoy V, Christensen MB, Fournelle JH, de Carlo F, Cohen S, Mahamid J, Scholl A, Young A, Doran A, Wilt FH, Coppersmith SN, Gilbert PUPA (2011) Self-sharpening mechanism of the sea urchin tooth. Adv Funct Mater 21(4):682–690
20. Zok FW, Miserez A (2007) Property maps for abrasion resistance of materials. Acta Mater 55(18):6365–6371
21. Bhushan B (1999) Principles and applications of tribology. Wiley, New York
22. Zhu XQ et al (2016) Multiple deformation mechanisms in the stone of a sea urchin tooth. Crystengcomm 18(30):5718–5723
23. Zaheri A, Nguyan H, Restrepo D, Daly D, Lin Z, Frank M, McKittrick J, Espinosa HD (2019) In situ wear study reveals role of microstructure on self-sharpening mechanism in sea urchin teeth. Submitted
24. Wang RZ, Addadi L, Weiner S (1997) Design strategies of sea urchin teeth: structure, composition and micromechanical relations to function. Philosophical Transactions of the Royal Society B-Biological Sciences 352(1352):469–480

**Publisher's Note** Springer Nature remains neutral with regard to jurisdictional claims in published maps and institutional affiliations.